A&A 501, 933–940 (2009)
DOI: 10.1051/0004-6361/200911964

Astronomy & Astrophysics

The parsec-scale properties of the radio galaxy 4C 26.42 in the dense cooling core cluster A1795

E. Liuzzo[1,2], G. B. Taylor[3,⋆], G. Giovannini[1,2], and M. Giroletti[1]

[1] Istituto di Radioastronomia, INAF, via Gobetti 101, 40129 Bologna, Italy
e-mail: liuzzo@ira.inaf.it
[2] Dipartimento di Astronomia, Università di Bologna, via Ranzani 1, 40127 Bologna, Italy
[3] Department of Physics and Astronomy, University of New Mexico, Albuquerque NM 87131, USA

Received 27 February 2009 / Accepted 9 May 2009

ABSTRACT

Aims. The aim of the present work is to study the radio emission on the parsec scale of 4C 26.42, the Brightest cluster galaxy in Abell 1795, in the framework of radiosources in a dense cool core cluster.
Methods. We present Very Long Baseline Array (VLBA) observations at 1.6, 5, 8.4 and 22 GHz. We performed a spectral index and multiepoch analysis.
Results. The source appears two-sided with a well defined and symmetric Z-structure at ∼5 mas from the core. The kiloparsec-scale morphology is similar to the parsec-scale structure, but reversed in PA, with symmetric 90° bends at about 2 arcsec from the nuclear region. Comparing data obtained at 3 different epochs we derive a 3σ limit to the apparent proper motion of $\beta_a < 0.04$. We suggest that the parsec-scale jets are sub-relativistic, in contrast with the high velocities found for most low-power radio galaxies. The origin of the unusual radio morphology remains a puzzle. We suggest that the identification of the parent galaxy with the central cD in a cooling cluster plays an important role in the properties and structure of the jets.

Key words. cooling flows – galaxies: clusters: individual: Abell 1795 – Galaxy: structure – radio continuum: galaxies – galaxies: nuclei

1. Introduction

Studies of central cluster galaxies show that amorphous and/or distorted radio sources are typical of the cooling cluster environment (O'Dea & Owen 1987; Taylor et al. 1994). Recently, using the high resolution imaging capabilities of the X-ray satellite Chandra, the interaction between the hot gas and the radio plasma in cooling clusters has become clearer, and it is now accepted that the intracluster gas and the central radio galaxy profoundly influence each other. Examples include Hydra A (McNamara et al. 2000) and Perseus A (Fabian et al. 2000). In both cases, there is an anti-coincidence between the radio lobes and X-ray emission. In particular, the kiloparsec radio lobes are located in X-ray cavities. Moreover Baum & O'Dea (1991) demonstrated that the central radio sources can arrest or slow down the cooling process. The central AGN can inject into the intra-cluster medium (ICM) an amount of energy comparable to that lost by the cooling X-ray gas.

High rotation Faraday measures (RMs) are frequently found toward radio sources at the centers of cooling core clusters. This is a direct consequence of the thermal gas and cluster magnetic fields present in the ICM. The detection of molecular gas (e.g., CO) and H_α emission confirms the presence in the ICM of dense cold gas as well. Baum & O'Dea (1991) and Sarazin et al. (1995) discussed a possible interaction between the radio sources and the cooling flow. For example, the disruption of the radio jets can be the consequence of the high-pressure ambient gas, which also explains the plume-like features of some sources.

At parsec-scale, there are well known sources in cooling core clusters like Hydra A (Taylor 1996), 3C 84 (Taylor et al. 2006a), PKS 1246-410 in Centaurus cluster (Taylor et al. 2006b); and PKS 2322-123 in A2597 (Taylor et al. 1999). All but one of these (PKS 1246-410) show two-sided structures and mildly relativistic jets. This is in sharp contrast to the predominately one-sided parsec-scale jets found in most low power radiogalaxies (Giovannini et al. 2001).

The radio galaxy 4C 26.42 (B2 1346+26) is identified with a very luminous ($M_v = -23$) cD galaxy at $z = 0.0633$. This cD galaxy is the brightest member of the rich cluster Abell 1795. In X-rays, A1795 shows a relaxed structure and it is one of the most powerful clusters of galaxies known, with a luminosity of $\sim 8.5 \times 10^{44}$ erg s^{-1} in the 0.5−4.5 keV band. A more recent Chandra study of Ettori et al. (2002) indicate that the central 200-kpc region is undergoing significant cooling with a gas mass deposition rate of about 100 $M_\odot$ yr^{-1} in the absence of any heating process. They also found that the shape of the potential is in agreement with the motion of the central dominant galaxy, and suggests that the central cluster region is not relaxed. It has a strong central peak of cooler gas and this evidence of "cooling flow" (Baum et al. 1992) is supported by the presence of strong emission-line nebulosity (Capetti et al. 2000; Fabian et al. 1994) around the central cD galaxy along with excess blue light. The blue light is probably due to massive stars (McNamara et al. 1996) with some contribution from young globular stars (Holtzman et al. 1996). Molecular gas in the cD galaxy has been detected through molecular hydrogen emission (Falcke et al. 1998). Fabian et al. (1994) observed in the core an X-ray filament that coincides with an H_α emission

⋆ Greg Taylor is also an Adjunct Astronomer at the National Radio Astronomy Observatory.

Table 1. Calibrators list.

Epoch yy-mm-dd	Frequency GHz	Observing time hour	Phase calibrators
03-08-07	1.6	1.0	J1350+3034
08-02-26	1.6	1.0	J1342+2709
97-04-06	5.0	1.0	J1350+3034
05-07-27	5.0	1.5	J1342+2709
08-02-26	5.0	1.5	J1342+2709
08-02-26	8.4	2.0	J1342+2709
08-02-26	22	3.5	J1342+2709

feature discovered by Cowie et al. (1983). This filament is produced by cooling gas from the ICM, and could be significant in improving our understanding of the energy and ionization source of the optical nebulosity, so frequently found in cooling core clusters.

High Faraday rotation measures (exceeding ~2000 rad m^{-2} in places) are found in 4C 26.42 in high resolution (0.6 arcsec) VLA images (Ge & Owen 1993). The magnitude and scale of the RM are consistent with a hot (~10^8) and dense (~0.03 cm^{-3}) X-ray emitting gas. The strength of the magnetic field is probably between 20 and 100 μG, depending on the degree of ordering.

From Very Large Array (VLA) observations, 4C 26.42 is known to have an FR I, Z-shaped small (2″ × 12″) radio morphology (van Breugel et al. 1984), with a total power at 0.4 GHz Log$P_{\rm tot,\,0.4\ GHz}$ = 25.47 W/Hz and a core power at 5 GHz Log$P_{\rm core,\,5\ GHz}$ = 23.70 W/Hz (Giovannini et al. 2005).

On the parsec-scale, Giovannini et al. (2005) observed 4C 26.42 at 5 GHz with the Very Long Baseline Array (VLBA). They found a faint peculiar structure with a total flux density of ~8 mJy, but the observations were inconclusive because of its low brightness. In this paper we discuss new multi-epochs, multi-frequencies VLBA observations of this source using the phase-referencing mode. In Sect. 2 we present the new data, in Sect. 3 we discuss the nuclear properties of this source. In Sect. 4 we discuss possible origins for the peculiar radio structures.

Throughout this paper, we assume H_0 = 70 km s^{-1} Mpc^{-1}, $\Omega_{\rm m}$ = 0.3, Ω_Λ = 0.7. At the distance of 4C 26.42, 1 mas corresponds to 1.2 pc.

2. Observations and data reduction

We obtained new VLBA observations at 1.6 GHz on 2003 August 07, at 5 GHz on 2005 July 27, and at 1.6, 5, 8.4 and 22 GHz on 2008 February 26 (see Table 1). Moreover we re-reduced the data at 5 GHz of 1997 April 4 (Giovannini et al. 2005). All data were obtained using the phase referencing mode, except for the 5 GHz data of 1997, whose quality largely improved after applying the improved source position obtained from the newer data taken using phase referencing. High resolution and high frequency data are necessary to study the nuclear region. Data at 1.6 and 5 GHz have the sensitivity and $(u-v)$ coverage necessary to study the more extended jet structure.

The observations were correlated in Socorro, NM. A total of 16 MHz bandwidth was recorded in both right and left circular polarization. Post-correlation processing used the NRAO AIPS package and the Caltech Difmap package. We followed the same scheme for the data reduction of all data sets. Using AIPS we applied ionospheric corrections and corrections to the Earth Orientation Parameters (EOPs). After this, we used the AIPS script VLBACALA to correct sampler offsets and to apply a-priori amplitude calibration. With VLBAPANG we corrected the antenna parallactic angles and with VLBAMPCL we removed the instrumental delay residuals. All calibrator data were also globally fringe-fitted and solutions were applied to the target sources with VLBAFRGP. After flagging bad visibilities, we obtained good models for the calibrators, which we used to improve the amplitude and phase calibration for the entire data set. Final maps were obtained with Difmap after averaging over IFs and in time. After editing, we applied multiple iterations of imaging and self-calibration in phase and amplitude. At last, to these improved quality data, we applied Modelfit to obtain the final set of components describing the data.

In Table 2 we report the image parameters for final natural weighting maps at different epochs and frequencies.

3. Results

3.1. The parsec scale structure

In Figs. 1–3 we present the full resolution images of 4C 26.42 at 1.6, 5, 8 and 22 GHz respectively. At low frequency and low resolution, the source shows two components (A and B) in the inner 15 mas (in PA ~ 60°) and two symmetric lobes oriented North−South (N1 and S1) with a peculiar Z shaped structure (Fig. 1, left). The source size is ~30 mas. At 5 GHz the two central components of the low resolution images are resolved into three components (A, C and B; see Fig. 1, right). The symmetric S1 and N1 lobes are still visible though with an extension of only ~10 mas. We note that components A and B are coincident with the regions where the jet position angle changes by ~90°. The parsec-scale structure is very symmetric. At still higher resolution (Fig. 2), we distinguish four components in the central 10 mas (A1, A2, C and B); N1 is completely resolved out while S1 is marginally detected. At the highest resolution, only the central components A1, A2 and C are visible (Fig. 3). We note that in high resolution images (8.4 and 22 GHz) because of the low signal to noise ratio the extended source structure is not visible in our images.

Comparing the parsec and kiloparsec structure (Fig. 4), we note that two changes in PA occur, one at ~15 mas from the core where PA goes from 60° to −30° and the second at ~2 arcsec where PA goes from −30° back to 60° to realign with the inner parsec-scale PA.

3.2. Modelfit results

Modelfitting was applied to all the data available for this source using elliptical, circular or delta components. The difmap modelfit program fits aggregates of various forms of model components, fitting directly to the real and imaginary parts of the observed visibilities using the powerful Levenberg-Marquardt non-linear least squares minimization technique. First we applied modelfitting to the last observations taken in 2008 independently for each frequency. All parameters of modelfit components were initially allowed to vary freely, however to facilitate comparisons between epochs, a mean shape was fixed for each frequency and only the position and flux density of the component was allowed to vary. We have also tried to describe elongated features with several small components. However, this resulted in an increase of χ^2, so we retained the simplest model. For example, in the case of S1 at 5 GHz (1997 April 6), the χ^2 increases from 1.393 (one component) to 1.709 (3 components). Following this step, we supposed that only the flux density of the components can change with the time. We fixed the shape of

Table 2. Image parameters for natural weighting maps.

Epoch	Frequency	Beam Size	Beam PA	Noise	Peak	Total flux density
yy-mm-dd	GHz	mas	deg	mJy beam^{-1}	mJy beam^{-1}	mJy
03-08-07	1.6	11.0 × 6.1	7	0.15	22.5	67.6
08-02-26	1.6	11.3 × 5.9	15	0.10	32.2	90.9
97-04-06	5	4.0 × 2.4	6	0.21	8.7	29.9
05-07-27	5	3.4 × 2.2	–8	0.13	10.0	42.0
08-02-26	5	3.0 × 1.5	–2	0.16	7.9	44.1
08-02-26	8.4	1.9 × 0.9	–4	0.08	7.0	25.2
08-02-26	22	1.0 × 0.7	–19	0.15	6.6	13.6

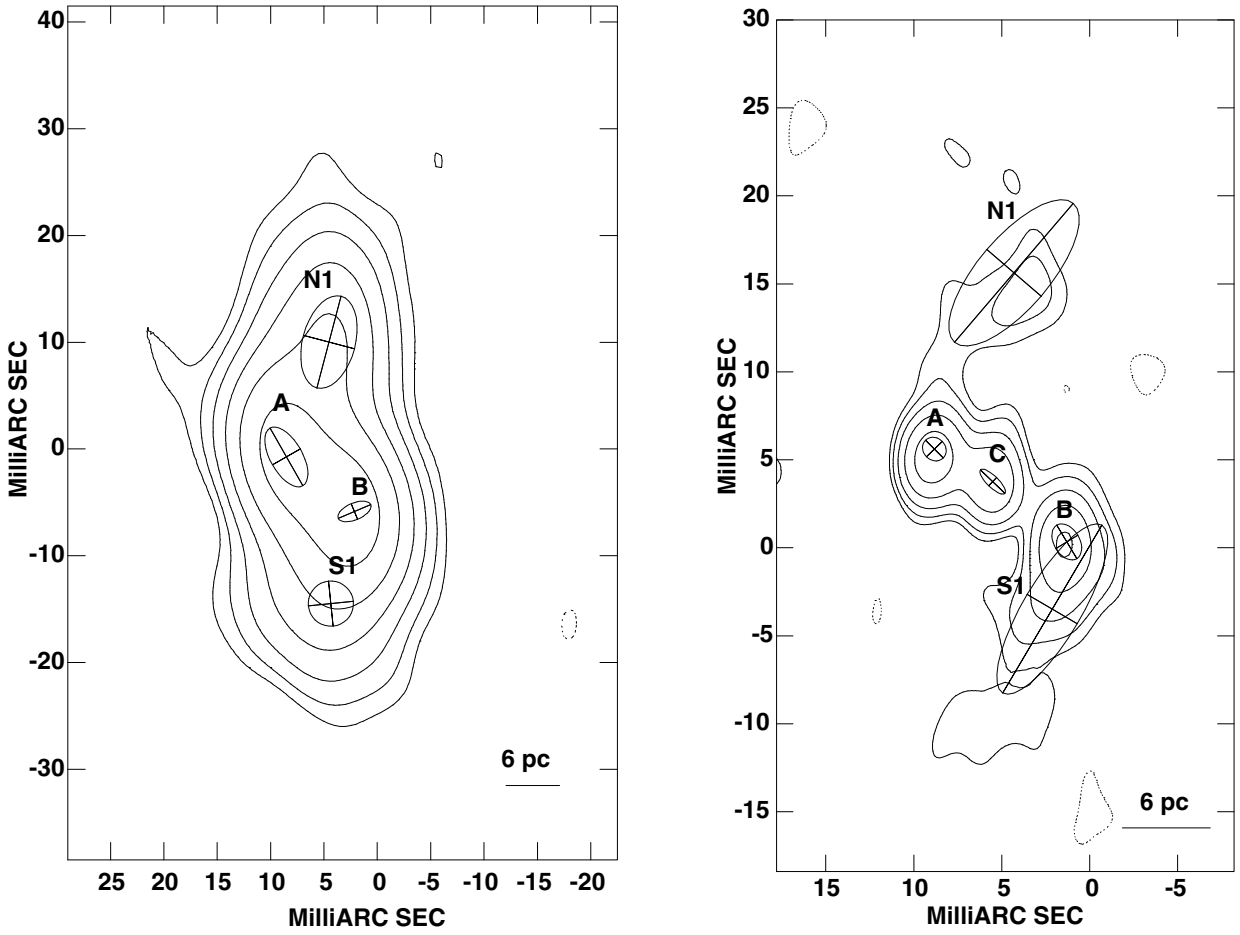

Fig. 1. On *the left*: 1.6 GHz VLBA contour map obtained on 2003 August. 07 with the 4 components given by modelfitting overlaid. The *HPBW* is 11.0 × 6.1 mas at 6.8° with a noise level =0.15 mJy/beam. Contours are: −0.45, 0.45, 0.9, 1.8, 3.6, 7.2, 14.4 mJy/beam. On *the right*: 5 GHz VLBA contour map obtained on 2005 July 27 with the 5 components given by modelfitting overlaid. The *HPBW* is 3.4 × 2.2 mas at −8.0° with a noise level =0.13 mJy/beam. Contours are: −0.4, 0.4, 0.8, 1.6, 3.2 and 6.4 mJy/beam.

the components and then modelled the (u, v) data from previous epochs at the corresponding frequencies.

In Table 3, we summarize the results obtained. For high frequencies (>1.6 GHz) we refer the component distance to component C because of symmetry reasons and its identification as the "core" of 4C 26.42 (see Sect. 3.4). At 1.6 GHz where the central component C is not visible, we use component A as the reference point. In Table 3 we give the frequency (Col. 1) and the epoch of observation (Col. 2), the χ^2 (Col. 3) of the fit, the name of the components (Col. 4), polar coordinates (r) and (θ) (Cols. 5 and 6) of the center of the component relative to the origin discussed above, with polar angle measured from the north through east, the positional uncertainty Δ (x, y) (Col. 7), the major axis a (Col. 8), the ratio b/a of minor b and major a axes (Col. 9) of the FWHM contour, the position angle Φ (Col. 10) of the major axis measured from north to east and the flux density S (Col. 11). Statistical errors are provided for the component parameters in Table 3. For elliptical and circular gaussian componentes we also calculated errors in size (a). Uncertainties in the sizes, positions and fluxes for components were derived from signal-to-noise ratios and component sizes (Fomalont 1999). True errors could be larger in the event that some components are covariant.

We note that the total flux density at 5 GHz, obtained by summing the different components in the 2008 epoch, is 44 mJy, therefore neglecting variability, only a small fraction (~17%) of the flux density is lost with respect to the sub-arcsecond core flux

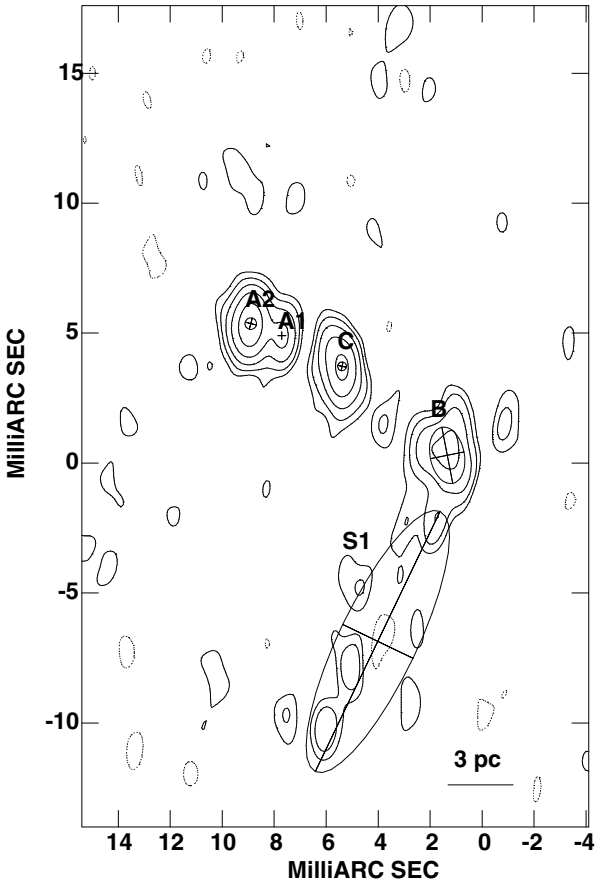

Fig. 2. 8.4 GHz VLBA contour map at the 2008 February 26 epoch with the 5 components derived from modelfitting overlaid. The *HPBW* is 1.86×0.86 mas at $-4.3°$ with a noise level =0.08 mJy/beam. Contours are: −0.25, 0.25, 0.5, 1, 2, 4 mJy/beam.

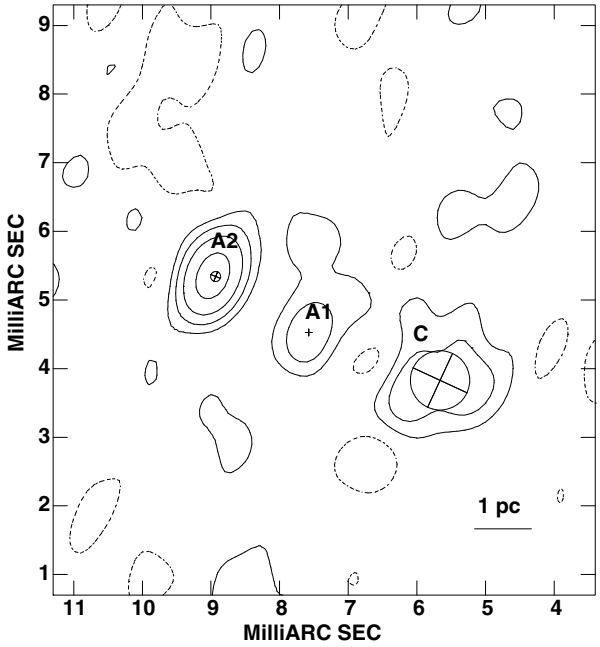

Fig. 3. 22 GHz VLBA contour map obtained on 2008 February 26 with the 3 components derived from modelfitting overlaid. The *HPBW* is 1.01×0.65 mas at $-18.5°$ with a noise level =0.15 mJy/beam. Contours are: −0.45, 0.45, 1.2, 2.4, 4.8 mJy/beam.

density (53 mJy) obtained from VLA data by van Breugel et al. (1984). Lower total flux density at 5 GHz of data carried out on 6 April 1997 are due to different not in phase referencing mode (see Sect. 2) observational analysis and it is not consequence of variability in the radioemission of the source. We compared the flux density of components A−C at different epochs at 5 GHz to search for possible variability (see Table 3). The flux density is slightly different but no clear trend is present. The limit on the amount of variability is ∼0.6 mJy at 3σ level (i.e. less that 10%). Improved sampling is necessary to better constrain variability.

We also have to note that, at higher frequencies, we lost flux density measurements of some components (see Table 3). This is a consequence of steep spectral index (see Table 4), low surface brightness of these (see Table 3) combined to probably not enough sensitivity of our images (see Table 2). Improved high quality images are necessary to give a complete spectral analysis of these components.

3.3. The parsec-scale spectrum

We used our multifrequency data from 2008 February 26 observations to study the spectral index (defined $S_\nu \propto \nu^{-\alpha}$) distribution of the parsec-scale structure. For our analysis, we first obtained images of the source using the same maximum and minimum baseline in the (u, v) coverage, the same griding and the same restoring beam. Then, we identified the different source components, and we measured their flux densities. Finally, we derived the spectral index for each component between 1.6 GHz and 5 GHz, 5 GHz and 8.4 GHz and between 8.4 GHz and 22 GHz (see Table 4).

Between 1.6 GHz and 5 GHz owing to the low resolution, single components are not well defined. The spectrum is in general steep as expected from low brightness extended components. We note that the steepest component is component B ($\alpha = 1.8$), and that the Northern extension (N1) is steeper, and more extended than S1.

At higher resolution, component C shows a flat spectrum ($\alpha_5^{8.4} \sim 0$, $\alpha_{8.4}^{22} \sim 0.14$) and it appears unresolved by a gaussian fit to the self-calibrated data. For these reasons and because of the source morphology, we identify C as the center of activity for 4C 26.42 with position RA $13^h48^m52\overset{s}{.}4894321 \pm 0.0000064$, Dec $26^d35^m34\overset{s}{.}340598 \pm 0.000038$ (estimated from the high resolution observations at 22 GHz of 2008 February 26). Also component A (with subcomponents A1 and A2) shows a clear flattening in the spectrum at high frequency, while component B despite the symmetric source morphology, has a steep spectrum (1.0) between 5 and 8.4 GHz, and as expected is not detected at 22 GHz. We do not interpret this steep spectrum as due to different synchrotron aging because the component N1 shows a steeper spectrum with respect to S1. Instead we suggest that the difference in spectral index is due to asymmetric interactions with the surrounding medium in the bending region. We note that the source is symmetric also on the kiloparsec-scale.

3.4. Jet dynamics

3.4.1. Proper motion

We studied the apparent proper motion of components A and B using the three different epochs at 5 GHz. We have observations at two different epochs also at 1.6 GHz, but the low resolution does not allow for a reliable search for possible proper motion. At 8.4 and 22 GHz only one epoch is available. We note that

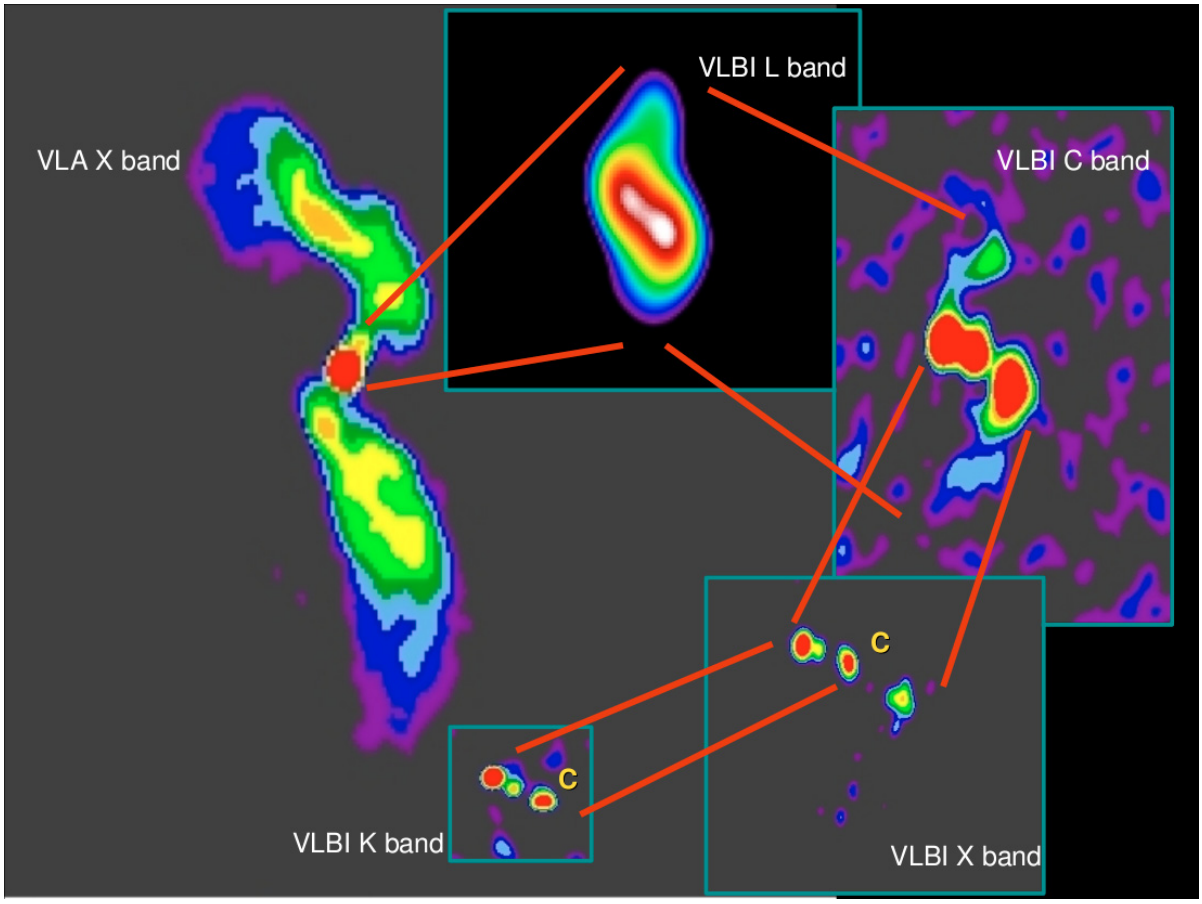

Fig. 4. Clockwise *from left to right*, zooming from kiloparsec to mas scale radiostructure of 4C 26.42: color maps of VLA *X* band, VLBI *L* band, VLBI *C* band, VLBI *X* band and VLBI *K* band data. (C) indicates the core component.

components A and B are well defined and their identification is not ambiguous, while components N1 and S1 are extended with no evident substructures so that their best fit position is affected by the varying sensitivity of different observations.

No significant proper motion was detected with a limits on the motion of A and B with respect to C of $\sim 9 \times 10^{-3}$ mas/yr ($\sim 3.6 \times 10^{-2}$c) at the 3σ level. Available data are poor (only 3 epochs) but with good time coverage (1997, 2005 and 2008 epochs). Therefore we conclude that A and B are stationary features, probably not due to moving knots in the jets but instead resulting from standing shocks in the region where the jet direction undergoes a symmetric PA change of about 90°.

3.4.2. Bulk velocity

An estimate of the jet bulk velocity rather than pattern speed can be derived from the jet to counter-jet brightness and size ratio, and by comparison of the nuclear with the total radio power (see e.g. Giovannini et al. 1988). The brightest component at 5 GHz at all epochs is A which is the nearest to C. The flux density ratio with respect to B at 5 GHz is $S_A/S_B \sim 1.4$. On the other hand, the distance ratio is $r_A/r_B \sim 0.8$. Moreover from an inspection of available images we note that an underlying jet connection between different structures (A−C) is not visible probably because of sensitivity limitations. In conclusion, there is no evidence of asymmetry in flux or position that would be expected from Doppler boosting.

In most FR I or FR II sources with good VLBI data a relatively simple nuclear-jet structure is present. The VLBI core shows a large fraction of the arcsecond core flux density, and the correlation between the core and total radio power can provide constraints on the jet velocity and orientation. In this source the arcsecond unresolved core shows a complex and extended structure in VLBI images which are not core dominated. The VLBI core is very faint and most of the flux density is from jet-like components or small regions reminiscent of radio lobes. Therefore it is not possible to estimate the jet velocity and orientation from the core dominance.

We can only note that the lack of underlying jets connecting the different knots, the source symmetry and the low power of the nuclear structure, all suggest that either the core structure of 4C 26.42 is near to the plane of the sky or/and the jets are not relativistic. This conclusion reinforces the identification of mas structures as standing shocks in the jet.

3.5. The physical conditions at equipartition

X-ray studies have shown that the black holes at the center of galaxy groups and clusters are capable of inflating cavities or "bubbles" in the surrounding X-ray emitting gas (Fabian et al. 2003, 2005; Birzan et al. 2004). The core of radio emission in 4C 26.42 is clearly identified with the highest X-ray brightness region and therefore with the center of the cluster. Similar to many recent examples in literature, the correspondence between the location of the radio lobes and X-ray cavities (Johnstone et al. 2002) suggests an expansion of the radio lobes into the surrounding X-ray emitting gas. In this section we compute the

Table 3. Results of Modelfit applied to 1.6, 5, 8.4 and 22 GHz data.

Frequency GHz	Epoch yy-mm-dd	χ^2	Component	r mas	θ deg	$\Delta(x,y)$ mas	a mas	b/a	Φ deg	S mJy
1.6	03-08-07	1.312	A, e	0	0	–	3.29 ± 0.02	0.5	29.6	24.9 ± 1.3
			N1, e	7.61	–130	0.02	6.20 ± 0.04	0.5	–67.3	21.4 ± 1.1
			B, e	10.58	–22	0.05	8.88 ± 0.10	0.6	–14.7	13.1 ± 0.7
			S1, c	14.11	–165	0.35	4.23 ± 0.07	1	–84.2	8.2 ± 0.4
1.6	08-02-26	1.001	A, e	0	0	–	3.29 ± 0.01	0.5	29.6	31.9 ± 1.6
			N1, e	8.08	–128	0.01	6.20 ± 0.02	0.5	–67.3	31.0 ± 1.6
			B, e	10.18	–17	0.02	8.89 ± 0.04	0.6	–14.7	21.4 ± 1.1
			S1, c	16.01	–178	0.03	4.23 ± 0.06	1	–84.2	6.6 ± 0.3
5	97-04-06	1.393	C, e	0	0	–	1.92 ± 0.05	0.3	45.7	7.6 ± 0.4
			A, e	4.02	64	0.15	1.43 ± 0.03	0.9	44.7	10.4 ± 0.6
			N1, e	11.19	–6	0.55	10.38 ± 1.09	0.4	–40.5	2.0 ± 0.2
			B, e	5.19	–130	0.03	2.21 ± 0.06	0.7	30.9	7.3 ± 0.4
			S1, e	9.4	–174	0.43	11.08 ± 0.86	0.3	–30.6	2.7 ± 0.2
5	05-07-27	1.205	C, e	0	0	–	1.92 ± 0.03	0.3	45.7	8.3 ± 0.4
			A, e	4.02	65	0.01	1.43 ± 0.02	0.9	44.7	11.9 ± 0.6
			N1, e	12.04	–4	0.13	10.38 ± 0.25	0.4	–40.5	5.3 ± 0.3
			B, e	5.07	–129	0.02	2.21 ± 0.03	0.7	31.0	8.4 ± 0.4
			S1, e	7.38	–158	0.09	11.08 ± 0.18	0.3	–30.6	8.1 ± 0.4
5	08-02-26	0.946	C, e	0	0	–	1.92 ± 0.03	0.3	45.7	9.3 ± 0.5
			A, e	4.02	64	0.01	1.43 ± 0.02	0.9	44.7	11.5 ± 0.6
			N1, e	11.10	–4	0.13	10.38 ± 0.23	0.4	–40.5	5.9 ± 0.3
			B, e	5.04	–127	0.02	2.21 ± 0.04	0.7	30.9	7.7 ± 0.4
			S1, e	6.85	–150	0.08	11.08 ± 0.15	0.3	–30.6	9.7 ± 0.5
8.4	08-02-26	0.890	C, c	0	0	–	0.34 ± 0.01	1	–11.9	5.3 ± 0.3
			A1, d	3.01	61	0.02	0	1	0	2.9 ± 0.2
			A2, c	4.02	63	0.01	0.44 ± 0.01	1	–14.7	8.1 ± 0.4
			B, e	5.09	–129	0.01	2.21 ± 0.02	0.6	11.0	7.5 ± 0.4
			S1, c	8.89	177	0.24	11.08 ± 0.47	0.3	–25.6	1.9 ± 0.1
22	08-02-26	1.040	C, c	0	0	–	0.9 ± 0.03	1	–25.0	4.6 ± 0.3
			A1, d	2.05	71	0.01	0	1	0	2.2 ± 0.2
			A2, c	4.04	65	0.01	0.15 ± 0.01	1	–21.8	6.8 ± 0.4

Parameters of each component of the model brightness distribution: Col. 1: frequency; Col. 2: epoch; Col. 3: (χ^2) of the fit; Col. 4: name of each component and we use (e) for elliptical gaussian component, (c) is for circular gaussian component, (d) for delta component; Col. 5: (r) and (θ), polar coordinates of the center of the component relative to an arbitrary origin, with polar angle measured from the north through east; Col. 6: $\Delta(x,y)$ position uncertainty, (–) indicates no error can be determined; Col. 7: (a) major axis; Col. 8: (b/a) ratio between minor (b) and major (a) axes of the FWHM contour; Col. 9: (Φ), position angle of the major axis measured from north to east; Col. 9: (S) flux density.

magnetic field strength, internal pressure, and total energy, assuming that equipartition conditions apply.

We use the standard formulae in Pacholczyk (1970), assuming that the relativistic particles and the magnetic field fully occupy the same volume ($\Phi = 1$), and that the amount of energy in heavy particles equals that in electrons ($k = 1$). We integrated over the frequency range 10^7–10^{11} Hz and we infer the extent of the source along the line-of-sight.

For the nuclear region imaged at 22 GHz (component C), we estimate a global equipartition magnetic field $H_{\rm eq} \sim 0.22$ Gauss. The total energy is $E_{\rm tot} \sim 6.9 \times 10^{52}$ erg, while the corresponding minimum internal pressure is $P_{\rm eq} \sim 2.4 \times 10^{-3}$ dyn/cm^2. For extended regions we used 1.6 GHz data and for the lobe on the north N1, we obtained $H_{\rm eq} \sim 1.73 \times 10^{-2}$ Gauss, $E_{\rm tot} \sim 1.6 \times 10^{53}$ erg and $P_{\rm eq} \sim 1.5 \times 10^{-5}$ dyn/cm^2. Instead for the lobe on the south S1, we obtained $H_{\rm eq} \sim 4.28 \times 10^{-2}$ Gauss, $E_{\rm tot} \sim 2.9 \times 10^{52}$ erg and $P_{\rm eq} \sim 8.9 \times 10^{-5}$ dyn/cm^2.

Birzan et al. (2004) estimated the energy required to inflate the large-scale bubbles in 4C 26.42. The energy required to create the observed bubble on the north in the X-ray emitting gas is $E_{\rm bubble} \sim 39 \times 10^{57}$ erg and the age of the bubble is $t_{\rm age} \sim 1.8 \times 10^7$ yrs, where $t_{\rm age}$ is $R/c_{\rm s}$ where R is the distance of the bubble center from the black hole and $c_{\rm s}$ is the adiabatic sound speed of the gas at the bubble radius. From these values we derive the required average jet mechanical power $P_{\rm jet} = E_{\rm bubble}/t_{\rm age}$ involved in "blowing" the bubble. We find $P_{\rm jet} \sim 6.9 \times 10^{43}$ erg/s ($\sim 6.9 \times 10^{36}$ W). Comparing the mechanical power of bubble with the heating necessary to prevent the gas from the cooling to low temperatures, Birzan et al. (2004) found that the cavities can balance the cooling if they are relativistic and non-adiabatic, and there may be further energy input if they are overpressured or produce a shock when they are formed.

We can compare $P_{\rm jet}$ derived above with the present parsec-scale jet power. Assuming for the northern jet a flux density upper limit of 20 mJy at 5 GHz, its bolometric radio power is $\sim 8 \times 10^{33}$ W, significantly lower than the power estimated from the Northern cavity and therefore indicating radiatively inefficient jets (0.1% of $P_{\rm jet}$). This result suggests that either the average jet power is much higher, possibly because of the presence of heavy particles, non-equipartition conditions, or an AGN activity that was higher in the past. We note that a heavy, slow jet is in agreement with the results discussed in Sect. 3.4. We also point out that low radiative efficiency seems to be a common theme for radio sources in clusters (Taylor et al. 2006b; Allen et al. 2006).

Table 4. Spectral index for single component.

ν_1-ν_2 GHz	*HPBW* mas×mas, °	Component	S_{ν_1} mJy	S_{ν_2} mJy	α
1.6–5	10.0 × 5.0, 0	A	15.4	7.5	0.63 ± 0.01
		B	29.0	3.6	1.82 ± 0.01
		N1	15.4	6.1	0.82 ± 0.02
		S1	9.4	7.3	0.66 ± 0.03
5–8.4	3.0 × 3.0, 0	A	6.7	6.7	0.00 ± 0.05
		C	4.1	4.1	0.00 ± 0.05
		B	6.2	3.7	1.03 ± 0.06
		S1	7.7	2.6	2.12 ± 0.06
8.4–22	1.86 × 0.86, –4	C	5.3	4.6	0.14 ± 0.04
		A1	2.9	2.2	0.29 ± 0.08
		A2	8.1	6.8	0.18 ± 0.03

S_{ν_1} and S_{ν_2} are referred to the flux density at lower ν_1 and higher ν_2 frequency between the two considered for the spectral analysis. All flux density values are derived from 2008 February 26 observations.

4. Discussion

The radio morphology on the parsec and kiloparsec scale of 4C 26.42 is very complex. From spectral index considerations and modelfitting results, we identify component C as the radio core. We note that the jets bend by ∼90° on scales of 10s of parsecs, and are remarkably symmetric. Two possibilities can explain the observed morphology in 4C 26.42: 1) if the pc scale jets are relativistic as in most radio galaxies (see e.g. Giovannini et al. 2001, 2005), and as suggested by unified models, this source has to be oriented at ∼90° with respect to the line-of-sight. In this case the large symmetric change in the source PA is real and not affected by projection. We find it difficult for a highly relativistic jet to survive such a large change in its orientation. Moreover we note that for a relativistic jet in the plane of the sky the Doppler factor is much lower than 1. Any decrease in the jet velocity will increase the Doppler factor and thereby manifest as an enhancement in the surface brightness. Since no clear surface brightness discontinuity is present in our images, we conclude that the jet velocity before and after the large PA change should be roughly the same. 2) Alternatively the source morphology suggests a subsonic flow which might be expected to have entrained thermal gas. This hypothesis is in agreement with the result that data at three different epochs do not show any proper motion, and with the identification of the bright regions on both sides of the core as bright standing shocks.

The presence of non-relativistic jets in this source is in sharp contrast with the observational evidence that parsec-scale jets in FR I radio galaxies are relativistic (Giovannini et al. 2001). In FR I radio galaxies relativistic jets in the parsec-scale region slow down because of interaction with the ISM on the sub-kiloparsec scale. However we must acknowledge the peculiar position and physical conditions of 4C 26.42 at the center of a cooling flow cluster. In Brightest Cluster Galaxies (BCGs) the presence of a dense ISM in the central (parsec-scale) regions is expected since the cooling flow is related to the presence of a high density gas as confirmed by the detection of CO line emission and molecular hydrogen (Edge 2001; Edge et al. 2002). Rossi et al. (2008) showed that a jet perturbation grows because of Kelvin-Helmotz instability and produces a strong interaction of the jet with the external medium with a consequent mixing and deceleration. The deceleration is more efficient increasing the density ratio between the ambient medium and the jet. Relativistic light jets are expected in FR I sources and the above effect can produce their slowing down from the parsec to the kiloparsec scale as found in many sources (Taylor 1996; Rossi et al. 2008). However a large value of the density ratio can produce a sub-relativistic and heavy jet even on parsec-scales as suggested by our data on 4C 26.42.

A strong interaction with the ISM could also explain the large difference in the spectral index distribution of the Northern and Southern region. The symmetric radio morphology suggests that the different spectral index distribution is related to an anisotropy in the ISM. We concluded in Sect. 3.4.2 that the mas structures result from standing shocks. Internal shocks can arise from sudden changes in the medium external to the jet. These shocks cause radiative losses through enhanced synchrotron radiation due to both increased particle energy density and magnetic field strength behind the shock. In particular, we note from Table 4 that the southern part (components B and S1) of 4C 26.42 is steeper than the northern part (components A and N1). This behaviour could be due to a denser ISM in the South than in the North region around our source.

We recall that in this source there are two dramatic changes in PA. A similar, but reverse change is present at about 2″ from the nuclear region. The origin of this peculiar morphology is not clear, but in any case requires the presence of heavy slow jets. A possible origin of a large symmetric change in the jet direction could be the interaction with a rotating disk as suggested by van Breugel et al. (1984) for 3C 293. In this model, a slow jet could be bent by ram pressure of a rotational motion of the accreted gas. The ISM of the galaxy rotates supersonically, so there is a stand-off cylindrical bow shock in the interstellar gas upstream of the jet. A result consistent with this scenario is the spettroscopic discovery in the nuclear region of 4C 26.42 of two clouds with a difference velocity of ∼330 km s^{-1}. Their emission line ratios of Hα and Hβ are very similar and typical of Liners exceptionally weak O [III] lines (Gonçalves et al. 1999). However, no clear evidence of rotating gas has been found. Moreover, the second change in direction would require two counter-rotating regions one near to the core and one at larger distance to explain the two changes in the jet direction.

An alternative possibility is that on the large scale the radio lobes rise buoyantly in the N-S direction according to the thermal gas distribution (see e.g. the radio X-ray overlay presented by Fabian et al. 2001). On intermediate scales, the jets have been heading out at PA −30° for a long time. Then, on the smallest scale, we can suppose that the radio jets have just been realigned recently due to the merger of a Binary Black Hole system which could produce a change in the nuclear jet ejection direction. Merritt& Ekers (2002) suggest that the orientation of a black hole's spin axis could change dramatically due to a merger event, leading to a sudden flip in the jet direction. Merger events are relatively common in cD galaxies, and in fact Johnstone et al. (1991) proposed that the structure in the envelope of the cD galaxy in A1795 is due to a merger with another giant galaxy. Alternatively the change of the jet PA on the parsec-scale could be due to a complex angular momentum of the gas accreted in the inner part of the disk of this galaxy, as proposed by Augusto et al. (2006) for B2151+174 (BCG of Abell 2390) or by rotating vortices in the cluster gas as Forman et al. (2009) suggested for the unique morphology of 3C 28, the BCG of Abell 115.

5. Conclusion

New sensitive, high resolution images at 1.6, 5, 8.4 and 22 GHz are presented for 4C 26.42, the radio loud BCG at the

center of the cooling flow cluster A1795. Our multi-frequency and multi-epoch VLBA observations reveal a complex, reflection-symmetric morphology over a scale of a few mas. No significant proper motion of observed components is found (Sect. 3.4). We identify the core (component C), along with two stationary shocks (A and B) and two lobes (N1 and S1). A strong interaction with the ISM can explain the spectral index distribution witch is steeper in the southern region of the source, and the presence of sub-relativistic and heavy jets on the parsec scale (Sect. 4). We note two 90° jet changes: one at ∼4−5 mas and one at 2″ from the nucleus. It seems plausible that the two 90° PA changes may have a different origin: we suggest buoyancy effects on the large scale, while on the mas scale it is difficult to identify if SMBH precession or peculiar gas motions are able to produce the sudden change in direction. To better investigate the peculiar structure of 4C 26.42, it would be useful to look at this source with a resolution in between that of the VLBA and VLA, as for example combining EVLA and e-Merlin data.

Acknowledgements. We thank the staff of NRAO involved in the observations for their help. NRAO is a facility of the National Science Foundation, operated under cooperative agreement by Associated Universities, Inc. This research has made use of the NASA/IPAC Extragalactic Data Base (NED), which is operated by the JPL, California Institute of Technology, under contract with the National Aeronautics and Space Administration. This research was partially supported by ASI-INAF CONTRACT I/088/6/0.

References

Allen, S. W., Dunn, R. J. H., Fabian, A. C., Taylor, G. B., & Reynolds, C. S. 2006, MNRAS, 372, 21
Augusto, P., Edge, A. C., & Chandler, C. J. 2006, MNRAS, 367, 366
Baum, S. A., & O'Dea, C. P. 1991, MNRAS, 250, 737
Baum, S. A., Heckman, T. M., & van Breugel, W. 1992, ApJ, 389, 208
Birzan, L., Rafferty, D. A., McNamara, B. R., et al. 2004, BAAS, 36, 905
Capetti, A., de Ruiter, H. R., Fanti, R., et al. 2000, A&A, 362, 871
Cowie, L. L., Hu, E. M., Jenkins, E. B., & York, D. G. 1983, ApJ, 272, 29
Edge, A. C. 2001, MNRAS, 328, 762
Edge, A. C., Wilman, R. J., Johnstone, R. M., et al. 2002, MNRAS, 337, 49
Ettori, S., Fabian, A. C., Allen, S. W., & Johnstone, R. M. 2002, MNRAS, 331, 635
Fabian, A. C., Canizares, C. R., & Boehringer, H. 1994, ApJ, 425, 40
Fabian, A. C., Sanders, J. S., Ettori, S., et al. 2000, MNRAS, 318, L65
Fabian, A. C., Sanders, J.-S., Ettori, S., et al. 2001, MNRAS, 321, L33
Fabian, A. C., Sanders, J. S., Crawford, C. S., et al. 2003, MNRAS, 344, L48
Fabian, A. C., Sanders, J. S., Taylor, G. B., & Allen, S. W. 2005, MNRAS, 360, L20
Falcke, H., Rieke, M. J., Rieke, G. H., Simpson, C., & Wilson, A. S. 1998, ApJ, 494, L155
Forman, W. R., et al. 2009, American Astronomical Society Meeting Abstracts, 213, #448.18
Fomalont, E. B. 1999, Synthesis Imaging in Radio Astronomy II, 180, 301
Ge, J. P., & Owen, F. N. 1993, AJ, 105, 778
Giovannini, G., Feretti, L., Gregorini, L., & Parma, P. 1988, A&A, 199, 73
Giovannini, G., Cotton, W. D., Feretti, L., Lara, L., & Venturi, T. 2001, ApJ, 552, 508
Giovannini, G., Taylor, G. B., Feretti, L., et al. 2005, ApJ, 618, 635
Gonçalves, A. C., Véron-Cetty, M.-P., & Véron, P. 1999, A&AS, 135, 437
Holtzman, J. A., Watson, A. M., Mould, J. R., et al. 1996, AJ, 112, 416
Johnstone, R. M., Naylor, T., & Fabian, A. C. 1991, MNRAS, 248, 18P
Johnstone, R. M., Allen, S. W., Fabian, A. C., & Sanders, J. S. 2002, MNRAS, 336, 299
McNamara, B. R., Jannuzi, B. T., Elston, R., Sarazin, C. L., & Wise, M. 1996, ApJ, 469, 66
McNamara, B. R., Wise, M., Nulsen, P. E. J., et al. 2000, ApJ, 534, L135
Merritt, D., & Ekers, R. D. 2002, Science, 297, 1310
O'Dea, C. P., & Owen, F. N. 1987, ApJ, 316, 95
Pacholczyk, A. G. 1970, Series of Books in Astronomy and Astrophysics (San Francisco: Freeman)
Rossi, P., Mignone, A., Bodo, G., Massaglia, S., & Ferrari, A. 2008, A&A, 488, 795
Sarazin, C. L., Burns, J. O., Roettiger, K., & McNamara, B. R. 1995, ApJ, 447, 559
Salomé, P., Combes, F., Edge, A. C., et al. 2006, A&A, 454, 437S
Taylor, G. B. 1996, ApJ, 470, 394
Taylor, G. B., Barton, E. J., & Ge, J. 1994, AJ, 107, 1942
Taylor, G. B., O'Dea, C. P., Peck, A. B., & Koekemoer, A. M. 1999, ApJ, 512, L27
Taylor, G. B., Gugliucci, N. E., Fabian, A. C., et al. 2006a, MNRAS, 368, 1500
Taylor, G. B., Sanders, J. S., Fabian, A. C., & Allen, S. W. 2006b, MNRAS, 365, 705
van Breugel, W., Heckman, T., & Miley, G. 1984, ApJ, 276, 79
Wilson, A. S., & Ulvestad, J. S. 1982, ApJ, 263, 576